Analytical Methods

ROYAL SOCIETY OF CHEMISTRY

PAPER

View Article Online
View Journal

Cite this: DOI: 10.1039/d4ay01432d

A label-free electrochemical biosensor based on a bimetallic organic framework for the detection of carbohydrate antigen 19-9†

Tongxiao Zhao and Baokang Jin *

Carbohydrate antigen 19-9 (CA19-9) is an important marker for pancreatic cancer, ovarian cancer and other tumors, and its rapid and stable detection is the basis for early diagnosis and treatment. In this paper, a label-free electrochemical immunosensor for the sensitive detection of CA19-9 has been developed. First, the synthesis of two novel core–shell bimetallic nanomaterials, namely Ce-MOF-on-Fe-MOF and Fe-MOF-on-Ce-MOF, was accomplished using the MOF-on-MOF approach. The poor electrical conductivity of MOF materials was addressed by incorporating polyethylenimide (PEI) functionalized rGO with Ce-MOF-on-Fe-MOF and Fe-MOF-on-Ce-MOF nanomaterials. Simultaneously, toluidine blue (Tb) was employed as a redox probe and physically adsorbed onto the synthesized materials, resulting in the formation of two nanomaterials: rGO@Ce-MOF-on-Fe-MOF@Tb and rGO@Fe-MOF-on-Ce-MOF@Tb. The fundamental characterization reveals that the sensing performance of the rGO@Ce-MOF-on-Fe-MOF@TB-based immune sensor surpasses that of the rGO@Fe-MOF-on-Ce-MOF@TB-based immune sensor, which is attributed to the fact that, unlike the interlayer-constrained structure of Fe-MOF-on-Ce-MOF, in Ce-MOF-on-Fe-MOF, Ce-MOF penetrates into Fe-MOF to form a heterogeneous structure due to the relatively large pore size of Fe-MOF, which better combines the excellent biocompatibility and strong anchoring effect of Fe MOFs on antibodies, as well as the high electrochemical activity and conductivity of Ce-MOF, to enhance sensing performance. The proposed label-free immunosensor based on rGO@Ce-MOF-on-Fe-MOF@Tb has a wide linear range (1–100 000 mU mL^{-1}), a low detection limit (0.34 mU mL^{-1}), good stability, reproducibility, and repeatability, and satisfactory applicability, which provides a potential platform for clinical applications.

Received 30th July 2024
Accepted 13th August 2024

DOI: 10.1039/d4ay01432d

rsc.li/methods

1. Introduction

Pancreatic cancer, a type of gastrointestinal tumor characterized by an insidious onset and the absence of typical early-stage symptoms, poses challenges in early diagnosis due to its high mortality rate. Consequently, patients are often diagnosed at advanced stages. The highly aggressive nature of pancreatic cancer and the dismal survival rate among patients make it a serious global burden of disease.[1] Early diagnosis is an effective way to treat and control pancreatic cancer. CA19-9 plays a pivotal role as a biomarker in screening individuals at high risk for pancreatic cancer and in the diagnostic assessment of cases.[2] Therefore, rapid and accurate detection of CA-199 is essential, and the routine methods for CA19-9 detection include the serum protein enzyme-linked immunization method, radioimmunoassay, and chemiluminescence.[3] Compared with these traditional analytical methods, the electrochemical immunoassay is easy to use and has high sensitivity.[4,5] In particular, label free electrochemical immunoassay is considered to be one of the most promising methods due to its simplicity, high sensitivity and low cost.[6,7] For example, based on 1D-MoS_2 nanorods/$LiNb_3O_8$ as signal amplification and polyoxometalate-incorporated gold nanoparticles as the sensor platform, a novel sandwich-type electrochemical immunosensor was developed for CA 19-9 detection. The quantification limit (LOQ) and the detection limit (LOD) values were obtained to be 0.10 μU mL^{-1} and 0.030 μU mL^{-1}.[8] In addition, an immunosensor made of CuBTC@N-GR@AuNPs@CS nanocomposites has been developed with a linear range of 10 μU mL^{-1} to 100 U mL^{-1} and a detection limit of 4.2 μU mL^{-1} was obtained.[9]

Metal–organic frameworks (MOFs) are porous materials made up of inorganic linkers and organic linker molecules. In recent years, the remarkable porosity, structural tunability, and excellent flexibility of MOF have garnered significant attention in gas storage, photocatalysis, and biomedicine. It is considered an excellent material for constructing DNA electrochemical biosensors due to its significant advantages such as large specific surface area, large pore size, and ease of functionalisation.[10,11] In particular, Fe-MOF-derived nanomaterials typically exhibit excellent

Department of Chemistry, Anhui University, Hefei 230601, China. E-mail: bkjinhf@aliyun.com

† Electronic supplementary information (ESI) available. See DOI: https://doi.org/10.1039/d4ay01432d

stability and are biocompatible and firmly anchored to antigen-antibodies.[12] However, a single MOF has fixed physical properties and poor electrochemical properties and may be prone to aggregation and poor solubility.[13] To this end, efforts have been made to ingeniously amalgamate two metals in order to acquire target materials with enhanced properties through synergistic effects. For instance, Xie *et al.*[14] synthesized Zr-MOF-on-Ce-MOF nanocomposites for the detection of ESAT-6 in nodules and Wang *et al.*[15] prepared Tb-MOF-on-Fe-MOF nanomaterials for the detection of CA-125. These bimetallic nanomaterials combine the advantages of two monometallic MOFs and exhibit excellent sensing properties compared to a single MOF. Based on the aforementioned work, we synthesized two novel core–shell bimetallic nanomaterials, namely Ce-MOF-on-Fe-MOF and Fe-MOF-on-Ce-MOF, utilizing the MOF-on-MOF approach employing biocompatible Fe-MOF and well-dispersed Ce-MOF. The inadequate electrical conductivity of most MOFs hinders their application in electrochemical sensing. However, using carbon materials in conjunction with MOFs has garnered significant attention due to their superior attributes, such as high electrical conductivity, excellent stability, and favorable biocompatibility.[16,17] Graphene (GO) is a two-dimensional structure of carbon atoms with large π-bonds and excellent electrical conductivity. Due to its significant advantages, including a large specific surface area, excellent thermal stability, exceptional electrical conductivity, ease of modification, and potential for large-scale production,[18–20] it is evident that this material holds immense potential for development in various fields such as polymer composite materials, biosensing, and biomedical health.[21–23] Therefore, we composite polyethyleneimine (PEI)-functionalized rGO with two nanomaterials, Ce-MOF-on-Fe-MOF and Fe-MOF-on-Ce-MOF, to compensate for the poor electrical conductivity of MOF materials. The redox probe toluidine blue (Tb) was concurrently employed and physically adsorbed onto the prepared materials to form two nanomaterials: rGO@Ce-MOF-on-Fe-MOF@Tb and rGO@Fe-MOF-on-Ce-MOF@Tb.

Based on the discussion above, in this study, novel nanocomposites of rGO@Ce-MOF-on-Fe-MOF@Tb and rGO@Fe-MOF-on-Ce-MOF@Tb were synthesized for the first time *via* a physical adsorption method and subsequently immobilized onto a glassy carbon electrode (GCE) to enable the detection of CA-199. The immune sensor based on rGO@Ce-MOF-on-Fe-MOF@Tb exhibits superior sensing performance compared to the immune sensor based on rGO@Fe-MOF-on-Ce-MOF@Tb. Tb serves as a redox probe to generate electrochemical signals, while the bimetallic CeFe-MOF combines the advantageous features of both Ce-MOF and Fe-MOF. This unique combination provides a large specific surface area, allowing more CA19-9 antibodies to be immobilized. Additionally, the incorporation of rGO significantly enhances the electrical conductivity of the material, thereby greatly improving the sensitivity of the immune sensor.

2. Experimental

2.1. Materials

NaCl, KCl, KH_2PO_4, Na_2HPO_4, $Ce(NO_3)_3\cdot 6H_2O$, $FeCl_3\cdot 6H_2O$, NaOH, 2-aminoterephthalic acid (NH_2-BDC), 1,3,5-benzenetricarboxylic acid (H_3BTC), bovine serum albumin (BSA) and polyvinyl pyrrolidone (PVP) were purchased from Shanghai Aladdin Reagent Co; HCl, $K_4Fe(CN)_6$, $K_3Fe(CN)_6$ and CH_3CH_2OH were provided by Sinopharm Chemical Reagent Co; GO, PEI and Tb were provided by Shanghai Maclin Biochemical; carcinoembryonic antigen (CEA), bovine serum albumin (BSA), human immunoglobulin G (IgG), CA-199 and the carbohydrate antibody (Ab-CA19-9) were purchased from Shanghai Bioengineering Technology Co. Human serum samples were provided by the First Affiliated Hospital of Anhui Medical University, and the serum CA19-9 content in the blank group was 0 mU mL^{-1}.

0.01 M phosphate buffer solution (PBS) solution preparation: NaCl 4 g, KCl 0.1 g, Na_2HPO_4 0.72 g, and KH_2PO_4 0.12 g were placed in a beaker, followed by pH adjustment using solutions of NaOH and HCl until reaching pH = 7.4. Finally, the volume was adjusted to 0.5 L. The deionized water used in the whole experiment was from a pure water system of Anhui Instrument (Ω = 18.2 MΩ cm^{-1}); the electrochemical impedance (EIS) solution consisted of a mixture of 5 mM $K_3[Fe(CN)_6]/K_4[Fe(CN)_6]$ and 0.1 M KCl solution; CA19-9 antibody solution (50 μg mL^{-1}) and CA19-9 antigen solution (1 KU mL^{-1}) master mix were prepared in PBS solution. A series of concentrations of antigen solution was prepared by dilution on this basis and stored at 4 °C.

2.2. Instruments

A pH meter (PHS-3C, Shanghai Leimagnet Co., Ltd); a supercentrifuge (Xiangyi Centrifuge Instrument Co. Ltd, Hunan, China); an electrochemical workstation (CHI 660D, CH Instrument Co. Ltd, Shanghai, China); an analytical balance (Huazhi Scientific Instrument Co. Ltd, Fujian, China); a scanning electron microscope (SEM-4800, Hitachi Ltd); a high-resolution transmission electron microscope (JEM-2100, JEOL, Japan); an X-ray photoelectron spectroscopy (XPS, ESCALAB 250Xi, America); an X-ray diffractometer (XRD, Smartlab 9kw, Japan); a Thales electrochemical work station (IM6, ZAHNER, Germany) were used.

2.3. Preparation of Ce-MOF

The synthesis of Ce-MOF was modified according to previous work.[24] The detailed procedure was conducted as follows: $Ce(NO_3)_3\cdot 6H_2O$ (324 mg, 0.75 mmol) was placed in a beaker and mixed with 15 mL of deionized water, followed by sonication for 5 minutes. Subsequently, H_3BTC (315 mg, 1.5 mmol) was dissolved in an equal volume of a water–ethanol mixture (15 mL), and the resulting solution of H_3BTC was added dropwise to the $Ce(NO_3)_3\cdot 6H_2O$ solution under magnetic stirring. The reaction mixture was then subjected to heating at 60 °C in a water bath for 2 hours. Finally, the obtained white precipitate was separated by centrifugation, washed thoroughly, and dried using a vacuum drying oven at 60 °C.

2.4. Preparation of Fe-MOF

Synthesis of Fe-MOF refers to the method in the literature[25] and has been slightly modified. Briefly, $FeCl_3 \cdot 6H_2O$ (100 mg, 0.369 mmol) was dissolved in 30 mL of DMF and sonicated for 5 minutes. Subsequently, H_2BDC (103 mg, 0.615 mmol) was added to the solution and sonicated until complete dissolution occurred. The resulting solution was then transferred into a Teflon-lined stainless steel autoclave (50 mL) and continuously heated at 110 °C for 24 hours. Finally, the reddish-brown precipitate obtained was thoroughly washed with absolute ethanol several times and dried in a vacuum drying oven at 60 °C.

2.5. Preparation of Ce-MOF-on-Fe-MOF and Fe-MOF-on-Ce-MOF

The Ce-MOF-on-Fe-MOF composite was prepared as follows, utilizing the obtained Fe-MOF as a template. The resulting Fe-MOF (120 mg) and PVP (120 mg) were incorporated into the preparation of Ce-MOF. Subsequently, the resultant precipitate underwent centrifugation, followed by multiple washes with ethanol and distilled water. Finally, the precipitate was subjected to vacuum drying at 60 °C in an oven.

The preparation of the Fe-MOF-on-Ce-MOF complex followed a similar procedure as that for Ce-MOF-on-Fe-MOF. Specifically, 120 mg of PVP was added to 120 mg of resulting Ce-MOF during the Fe-MOF preparation. The resulting suspension, exhibiting a red-brown color, underwent centrifugation and subsequent washing steps. Finally, the obtained precipitate was dried at 60 °C under vacuum conditions.

2.6. Preparation of rGO@Ce-MOF@Tb, rGO@Fe-MOF@Tb, rGO@Ce-MOF-on-Fe-MOF@Tb and rGO@Fe-MOF-on-Ce-MOF@Tb nanocomplexes

Initially, 30 mg of reduced graphene oxide GO was dissolved in 20 mL of ethanol. Subsequently, 8 mL of the 1% PEI solution was added dropwise to the GO solution and stirred for 2 hours at room temperature, resulting in a solution denoted as Solution A. In another container, 20 mg of Ce-MOF/Fe-MOF/Ce-MoF-on-Fe-MOF/Fe-MoF-on-Ce-MOF was dispersed in 20 mL of deionized water, and solution B was obtained after 5 minutes of ultrasonic treatment. Then suspension B was added to solution A and stirred for another 12 hours. Finally, a Tb solution (1.5 mg mL^{-1}) consisting of 20 mL volume was gradually introduced into the aforementioned mixture and further stirred for another period of 12 hours. The resultant suspension underwent multiple centrifugation washes before being dried in a vacuum drying oven at a temperature of 60 °C. Ultimately, the composites comprising rGO@Ce-MOF@Tb, rGO@Fe-MOF@Tb, rGO@Ce-MOF-on-Fe-MOF@Tb, and rGO@Fe-MOF-on-Ce-MOF@Tb were obtained (Scheme 1A).

2.7. Preparation of immunosensors

The GCE was polished successively with 1.0 μm, 0.3 μm, and 0.05 μm alumina powders, followed by thorough sonication in deionized water, ethanol, and deionized water for cleaning purposes. Subsequently, the electrode was immersed in a solution of 0.5 M H_2SO_4 and activated within the potential range of −1.0 V to 1.2 V until achieving a stable and reproducible cyclic

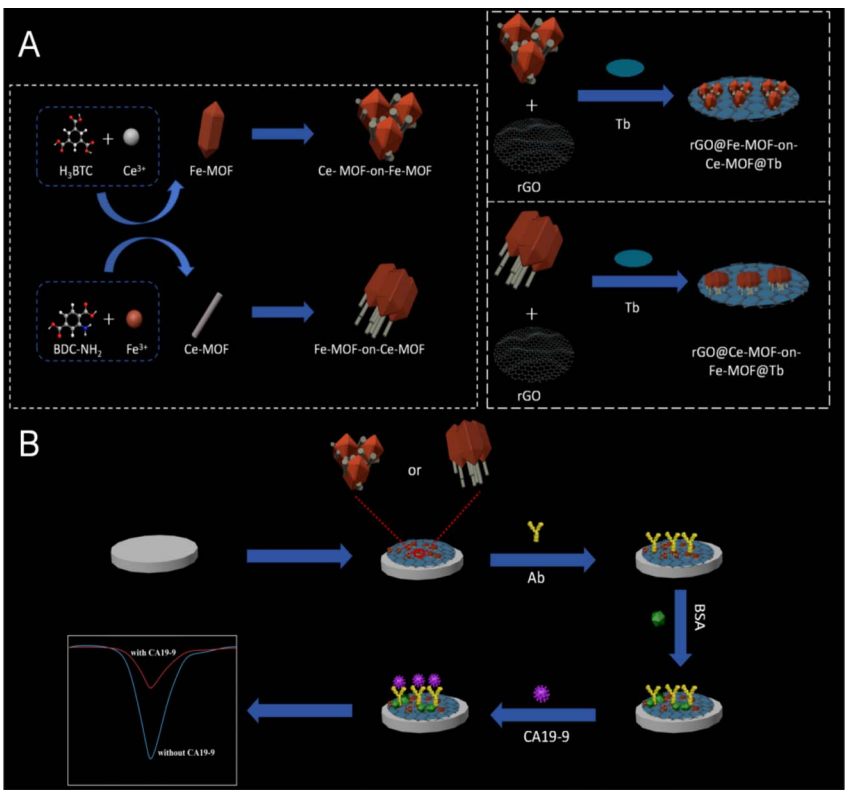

Scheme 1 Schematic diagram of an electrochemical immunosensor.

voltammogram. Finally, the electrodes were rinsed with ultrapure water and air-dried for subsequent utilization. A 10 μL drop of rGO@Ce-MOF-on-Fe-MOF@Tb solution was taken on the surface of the GCE and dried in air for 3 h. Subsequently, 10 μL of Ab-CA19-9 (10 mg mL^{-1}) was added dropwise on the surface of the GCE and incubated at 4 °C for 12 h. The electrodes were washed with PBS to remove unbound Ab and blown dry with N_2. To prevent the leakage of non-specific adsorption sites, 10 μL of BSA (1%) was added dropwise to the electrode surface and incubated at 37 °C for 2 h. The electrode was washed and blown dry with PBS solution and stored at 4 °C. For comparison, immunosensors based on rGO@Ce-MOF@Tb, rGO@Ce-MOF-on-Fe-MOF@Tb, and rGO@Fe-MOF-on-Ce-MOF@Tb were prepared in the same way. The preparation steps of the electrochemical bioimmunosensor are shown in Scheme 1B.

2.8. Electrochemical determination of CA19-9

All electrochemical measurements were performed at room temperature, and a conventional three-electrode system was used. A modified glassy carbon electrode served as the working electrode, while a platinum wire electrode was employed as the counter electrode. Additionally, a saturated calomel electrode was utilized as the reference electrode. Quantitative analysis was performed using differential pulse voltammetry (DPV).

The cyclic voltammetry (CV) technique was employed in a 0.01 M phosphate-buffered saline (PBS) solution at pH = 7.4, with the potential range set from −0.6 V to 0.1 V and a scan rate of 100 mV s^{-1}. The DPV method was conducted in a 0.01 M PBS solution at pH = 7.4, starting from an initial potential of −0.6 V and terminating at 0.1 V, using an amplitude of 50 mV and a pulse width of 0.05 s. Electrochemical impedance spectroscopy (EIS) measurements were performed in a mixed solution containing equal concentrations of $[Fe(CN)_6]^{3-}$ and $[Fe(CN)_6]^{4-}$ ions (5 mM each), dissolved in KCl with a concentration of 0.1 M. The EIS experiments were carried out using a Thales electrochemical workstation over the frequency range from 0.l kHz to l00 kHz, applying a signal amplitude of 5 mV.

3. Results and discussion

3.1. Chemical structure and components of MOFs

The successful synthesis of Ce-MOF, Fe-MOF, Ce-MOF-on-Fe-MOF, and Fe-MOF-on-Ce-MOF was confirmed through XRD, FT-IR, and XPS characterization techniques. The crystal structures of the four materials were characterized by XRD. The main diffraction peaks (Fig. S1A†) observed for Fe-MOF appeared at $2\theta = 8.5°$, 9.5°, 18.4°, and 22.1°, respectively, corresponding to the crystal planes (002), (101), (200), and (201). These peaks exhibit similarities with the reported MIL-101 family patterns in the literature. However, their intensities are relatively lower suggesting a lower crystallinity of the synthesized Fe-MOF. The XRD pattern of the prepared Ce-MOF exhibited a resemblance to the peak reported in the literature,[26] indicating successful synthesis of Ce-MOF. The sharpness of the XRD peaks suggested a high degree of crystallinity in the sample. Furthermore, the XRD results for Ce-MOF-on-Fe-MOF showed similarities with those obtained for Fe-MOF alone, while the XRD pattern observed for Fe-MOF-on-Ce-MOF resembled that of pure Ce-MOF. This can be attributed to limitations in thickness when characterizing these composites using XRD.[27]

The chemical bonds of the materials were characterized using FT-IR, and similar results were obtained. As shown in Fig. S1B,† for determining Fe-MOF and Ce-MOF-on-Fe-MOF composites, absorption peaks at 750, 1250, 1402, 1586, and 1685 cm^{-1} represent characteristic peaks of the amino group. The absorption peak at 750 cm^{-1} is attributed to the deformation vibration of the C–H bond in the benzene ring. Two peaks at 1383 and 1640 cm^{-1} are attributed to C–O and C═O stretching vibrations respectively; these results are consistent with previously reported literature.[28] In measurements of Ce-MOF and Fe-MOF-on-Ce-MOF composites, stretching vibrations at around 3344 cm^{-1} and 3390 cm^{-1} belong to water molecule O–H stretching vibrations in MOFs. Absorption peaks at 1611–1556 cm^{-1} and 1435–1372 cm^{-1} are attributed to asymmetric/symmetric stretching vibrations of –COO–,[29] while an absorption peak at 534 cm^{-1} corresponds to the Ce–O stretching vibration.[30]

In addition, XPS analysis was conducted to further investigate the chemical structures and elemental valence states of the four composites: Ce-MOF, Fe-MOF, Ce-MOF-on-Fe-MOF, and Fe-MOF-on-Ce-MOF (Fig. S2A†). The XPS full-scan spectra of Ce-MOF revealed characteristic signals of C 1s, O 1s, N 1s, and Ce 3d (Fig. 2A). Additionally, the C 1s map displayed distinct peak morphologies at 284.8 eV (C–C bonds), 285.9 eV (C–O bonds), and 288.7 eV (COO bonds)[31] (Fig. S2B†). The peaks of the binding energies at 881.7 eV, 885.3 eV and 900.3 eV, 903.9 eV mainly correspond to the Ce 3d 5/2 and Ce $3d_{3/2}$ states,[32] while the peaks at 881.7 eV and 900.3 eV are associated with Ce^{4+}. The peaks of 885.3 eV and 903.9 eV were associated with Ce^{3+}.[33] These results all indicate the successful preparation of Ce-MOF. The XPS full-scan spectrum of Fe-MOF in Fig. S2D† displays characteristic signals for C 1s, O 1s, N 1s, and Fe 2p. In Fig. S2E,† the C 1s map reveals distinct carbon forms at binding energies of 284.8 eV (C–C), 286.0 eV (C–O), and 288.7 eV (COO). The peaks observed at binding energies of 712.2 eV, 713.7 eV, 725.3 eV, and 726.8 eV predominantly correspond to the Fe $2p_{3/2}$ and Fe $2p_{1/2}$ states respectively. The peaks at 712.2 eV and 725.3 eV are associated with Fe^{2+}, while the peaks at 713.7 eV and 726.8 eV are associated with Fe^{3+}; these findings are consistent with previous literature reports.[34]

For Ce-MOF-on-Fe-MOF, the high-resolution XPS spectra of Ce 3d show the coexistence of Ce^{3+} and Ce^{4+} ions (Fig. 1A). However, the Fe 2p signal is poor (Fig. 1B). The Fe-MOF layer is covered by the Ce-MOF layer in Ce-MOF-on-Fb-MOF, resulting in a poor signal for the Fe element. In contrast, a clear Fe 2p signal appeared in Fe-MOF-on-Ce-MOF spectra (Fig. 1D), in which the coexistence of Fe^{2+} and Fe^{3+} ions was observed. However, no substantial Ce 3d signal was observed. This is because only the structure of the nanomaterial surface can be probed by XRD and XPS characterization. The presence of a Ce 3d signal in Ce-MOF-on-Fe-MOF materials indicates that Ce-MOF penetrates into Fe-MOF, leading to the complete

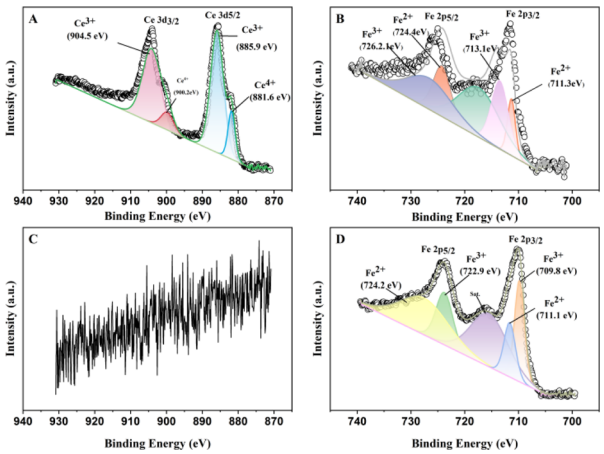

Fig. 1 High-resolution Ce 3d and Fe 2p XPS spectra of (A and B) Ce-MOF-on-Fe-MOF and (C and D) Fe-MOF-on-Ce-MOF.

integration of Ce-MOF with Fe-MOF. In contrast, Fe-MOF cannot penetrate into Ce-MOF because the pore size of the former is larger than that of the latter, and Fe-MOF can only cover the upper surface of Ce-MOF.[35]

3.2. Surface morphology of MOFs

The SEM image of Fe-MOF exhibited a uniform polyhedral morphology, and its surface displayed a relatively rough texture (Fig. S4A†). The TEM image revealed that the nanoparticles had an average size of approximately 0.5 μm (Fig. S4B†). However, due to the low crystallinity, no discernible lattice structure was observed in the high-resolution TEM image (Fig. S4C†).

The SEM images show that Ce-MOF has a stick-like structure and a relatively smooth surface (Fig. S4D†). The average diameter of Ce-MOF is about 80 nm (Fig. S4E†). As shown in Fig. S4F,† analyzing the HR-TEM images of the samples shows that the lattice stripe spacing of the samples is 0.256 nm, which corresponds well to the (141) crystal surface of CeO_2.

The SEM and TEM images reveal the successful synthesis of Ce-MOF-on-Fe-MOF, as evidenced by the embedding of Ce-MOF within numerous polyhedral Fe-MOF structures (Fig. 2A and B). Furthermore, HR-TEM images exhibit distinct heterostructures (Fig. 2C). In the case of Fe-MOF-on-Ce-MOF, the original larger-sized polyhedron structure transforms into a smaller irregular shape upon Ce-MOF. Additionally, various nanoparticles are observed to be attached to the surface of Ce-MOF (Fig. 2D). This structural alteration is further supported by TEM analysis (Fig. 2E), indicating that Ce-MOF exerts a negative influence on crystallization behavior during Fe-MOF synthesis.

In Fig. S5,† it can be observed that Fe-MOF, Ce-MOF, Ce-MOF-on-Fe-MOF and Fe-MOF-on-Ce-MOF are randomly attached to the surface of thin-layered rGO. The successful synthesis of rGO@Fe-MOF@Tb, rGO@Ce-MOF@Tb, rGO@Ce-MOF-on-Fe-MOF@Tb, and rGO@Fe-MOF-on-Ce-MOF@Tb nano-complexes has been demonstrated.

3.3. Electrochemical characterization of MOFs and their composites

EIS is used to study the interfacial properties of modified electrodes, and the Nyquist diagram consists of two parts: a low-frequency linear part, which is associated with diffusion-limited electrochemical behavior, and a high-frequency semicircular part, which is associated with electrical and chemical processes controlled by electron transfer.[36]

The inset, shown in Fig. S6,† shows a Randles equivalent circuit diagram, which represents each of the components at the working electrode interface and in solution: solution resistance (R_s), charge transfer resistance (R_{ct}), double layer capacitance (C_{dl}), and Warburg impedance (Z_w).[37] In the Nyquist diagram, the diameter of the semicircle in the impedance curve is proportional to R_{ct}, which reflects electron transfer efficiency at the electrode–electrolyte interface. As shown in Fig. S6,† EIS was employed to characterize nanocomposite preparation processes. The Nyquist diagrams of different electrodes indicate that the bare electrode has the smallest semicircle diameter and thus exhibits good conductivity with low Rct. After loading the MOF material onto the GCE, Rct increases due to the weak electrochemical conductivity of the MOF layer, which inhibits

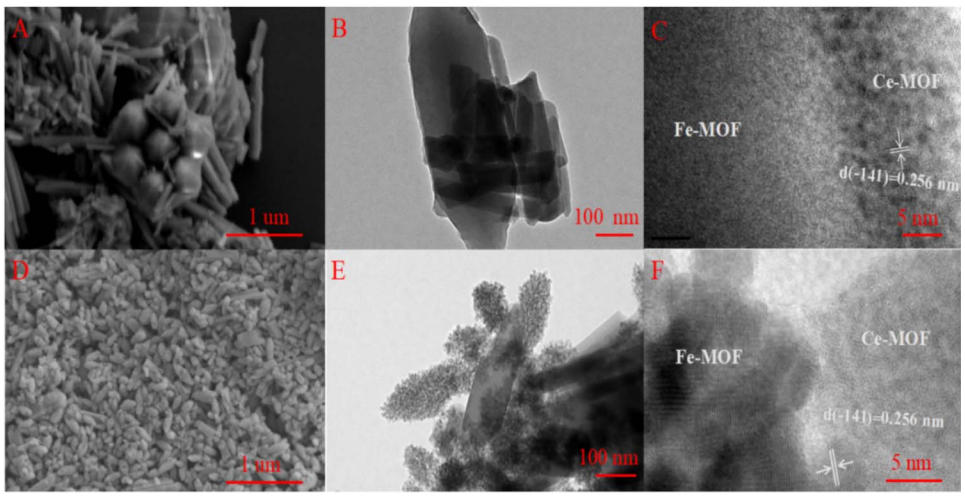

Fig. 2 SEM, TEM and HR-TEM images of (A–C) Ce-MOF-on-Fe-MOF and (D–F) Fe-MOF-on-Ce-MOF.

electron transfer at the electrolyte–electrode interface. However, the introduction of rGO leads to a decrease in R_{ct}, attributed to its high electrical conductivity, which promotes electron transfer and indicates the successful preparation of composite nanomaterials.

It is well known that the difference in Rct values induced by each step can be used to assess the conductivity of a material. Observing the glassy carbon electrodes modified with the four MOF materials (Fig. S6†), it was found that the modification of Fe-MOF on the bare GCE resulted in the highest increase in Rct values, indicating that Fe-MOF has the worst conductivity. In contrast, Ce-MOF-on-Fe-MOF modified electrodes showed the slightest change in the Rct value, suggesting that their conductivity is better than that of the above single MOF due to the role of the heterostructure in promoting electron transfer.[38] The conductivity of Fe-MOF-on-Ce-MOF is less than that of single Ce-MOF, which is attributed to the fact that Fe-MOF is covered on the surface of Ce-MOF, which inhibits the electron transfer.

To determine the oxidation reaction control mechanism of the composite nanomaterials on the GCE, the effects of the scan rate, peak current, and peak potential were individually investigated in this experiment. Fe-MOF was excluded from the investigation due to its poor conductivity and lack of electrochemical signals in the CV curve. As depicted in Fig. S7,† both anodic and cathodic oxidation peak currents of all three composites gradually increased with increasing scan rates within the range of 10–150 mV s^{-1}. Furthermore, a linear relationship between current and the scanning rate was observed for all three composites, indicating that surface-controlled electron transfer processes govern their behavior.[39]

3.4. Electrochemical characterisation of immunosensor preparation processes

As shown in Fig. 3A, CV was used to validate each step of the sensor construction process. It was observed that the bare GCE did not have any significant redox peaks during the linear scan in PBS solution, which was attributed to the fact that it was not loaded with electroactive substances. After loading Ce-MOF-on-Fe-MOF, a pair of typical redox peaks appeared, with an oxidation peak current value of 300 μA and an $E^{\theta\prime}$. Potential ($E^{\theta\prime} = 1/2$ ($E_{ox} + E_{red}$)) of −0.22, which was clearly derived from the redox reaction of Tb. After incubation with Ab, the redox current appeared to drop to 180 μA, which was attributed to the immobilization of the protein hindering electron transfer; similarly, further incubation with the inactive substance BSA resulted in a further decrease in a current of 60 μA, and the peak current continued to drop after incubation with CA19-9. The CV measurements indicated that each step of the construction of the immunosensors was successful.

The DPV profiles of the GCE for each modification step, as presented in Fig. 3B, provide reliable evidence of the successful construction of the immunosensors. The bare GCE, devoid of electroactive substances, exhibited no electrochemical signals. In contrast, the Ce-MOF-on-Fe-MOF-modified electrode displayed a distinct peak current signal, a clear indication of successful modification. The subsequent modifications with Ab, BSA, and CA19-9 sequentially decreased the current response, further confirming the successful construction of the immunosensors. The change in peak current of the Ce-MOF-on-Fe-MOF-modified electrode serves as a reliable electrochemical signal for CA19-9 detection.

EIS was also used to validate the successful preparation of the immunosensor, as shown in curve Fig. 3C. The bare GCE

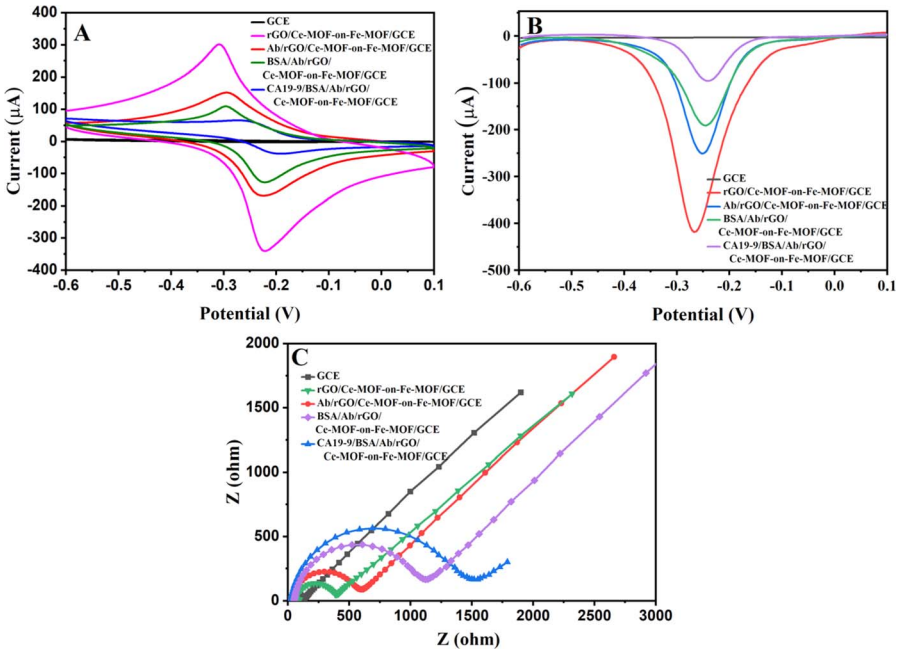

Fig. 3 (A) CV, (B) DPV and (C) EIS study for each immobilization step. CV and DPV were conducted in 0.01 M PBS (pH = 7), and EIS was performed in 5.0 mM $[Fe(CN)6]^{3-/4-}$ containing 0.01 M KCl electrolyte solution.

exhibits a minimal semicircular shape, which is mainly diffusion-limited during the electrochemical process. The modification of the electrode interface using Ce-MOF-on-Fe-MOF resulted in an increase in Rct, indicating that Ce-MOF-on-Fe-MOF was successfully immobilized on the GCE. After incubation with Ab, the radius of the semicircular region increased significantly, indicating that Ab was immobilized, which was attributed to the fact that the diffusion of ferrocyanide to the electrode surface was impeded by the protein layer formed on the electrode surface. The resistance increased gradually after the BSA sealing. After incubation with CA19-9, the resistance increased further, proving the successful specific recognition between CA19-9 antigen and CA19-9 antibody.

Similarly, as shown in Fig. S8,† the construction process of rGO@Ce-MOF@Tb and rGO@Fe-MOF-on-Ce-MOF@Tb-based immunosensors was consistent with that of the rGO@Ce-MOF@Tb-based immunosensors. Based on their CV, DPV and EIS data, a comparable trend to that observed in the rGO@Ce-MOF@Tb-based immunosensor can be inferred, indicating successful preparation of all three aforementioned immunosensors. For comparative analysis, Table S1† summarizes the peak current values obtained from these three immunosensors.

It can be seen that with the modification of the bare GCE with different nanocomposites, immobilization of Ab, sealing of BSA, and the detection order of CA 199, the oxidation peak current value decreases accordingly. It is well-known that the variation in peak current values resulting from each step reflects the loading of the added layer. Therefore, the sensing performance of the three immunosensors was evaluated based on the relative change in peak current values at each step, specifically by comparing the difference in peak current values before and after coating with a new layer. Among these immunosensors, it was found that modification of rGO@Ce-MOF-on-Fe-MOF@Tb on the bare GCE resulted in the highest oxidation peak current value, indicating superior conductivity. In contrast, the rGO@Fe-MOF-on-Ce-MOF@Tb modified electrode has the smallest value of oxidation peak current, indicating the worst conductivity. As shown in Fig S9,† the change in oxidation peak current after incubation of Ab by the three immunosensors was observed, and it was found that the rGO@Ce-MOF-on-Fe-MOF@Tb immunosensor showed the largest change in oxidation peak current (150 μA), implying that it was loaded with a lot of Ab, while rGO@Ce-MOF@Tb showed the smallest amount, which suggests that the heterogeneous structure is favorable for the immobilization of Ab. After incubating CA19-9 in a BSA solution and subsequent cleaning with PBS, the peak current of the rGO@Ce-MOF-on-Fe-MOF@Tb immunosensor exhibited the most significant change (100 μA). This observation suggests that an abundant amount of antibody was effectively immobilized on the rGO@Ce-MOF-on-Fe-MOF@Tb surface, enabling specific binding between CA19-9 and its corresponding antibody. In summary, the rGO@Ce-MOF-on-Fe-MOF@Tb immunosensor has the best electrical conductivity and immobilizes more Ab. All these results confirm that the rGO@Ce-MOF-on-Fe-MOF@Tb-based immunosensor exhibits better sensing performance than other immunosensors.

3.5. Optimizing response conditions for immunosensors

The immunosensor achieved optimal detection performance through the optimization of experimental conditions, including pH value adjustment in the test solution, substrate material rGO@Ce-MOF-on-Fe-MOF@Tb concentration control, and manipulation of CA19-9 incubation temperature and time. The experimental results are illustrated in Fig. S10.†

The pH value, a key determinant of protein activity, plays a pivotal role in shaping the response signal of the immunosensor. As shown in Fig. S10A,† the modified electrode achieved its optimal current response at a pH of 7. Given that extreme acidic or basic conditions can cause denaturation of antigens and antibodies, we selected PBS with a pH of 7 as the test solution for subsequent experiments, ensuring the best sensing performance.

The concentration and volume of the modified electrode material are the key factors affecting the electron transfer ability of the immunosensor. As depicted in Fig. S10B and C,† a significant increase in the signal was observed at concentrations of 1–3 mg mL^{-1} and volumes of 7–10 μL. However, further increases in the concentration and volume lead to a decline in the signal, possibly due to the increased thickness of the material impeding electron transfer.[40] Therefore, we chose a concentration of 3 mg mL^{-1} and a volume of 10 μL for follow-up experiments.

The specific binding of antigen and antibody in immunosensors is significantly influenced by the incubation time and temperature, thereby impacting their performance (Fig. S10D†). The electrochemical signal exhibited a decreasing trend as the temperature increased within the range of 4 °C to 37 °C, reaching its minimum at 37 °C. However, beyond 37 °C, peak current increased due to reduced antigen–antibody activity at extreme temperatures, hindering immune complex formation. Consequently, an optimal incubation temperature of 37 °C was selected. Moreover, Fig. S10E† demonstrates that the oxidation peak current experienced a substantial decline during the first hour (30–60 min) before stabilizing, indicating saturation of immune complex binding after a 60-minute incubation period. Henceforth, this duration was determined as the optimal incubation time for Ab with CA19-9.

3.6. Performance of the immunosensor

DPV tests were performed under the above-optimized conditions to assess the performance of the immunosensor for detecting CA19-9. As shown in Fig. 4, the oxidation peak current decreases as the concentration of CA19-9 increases. This is because the formation of immune complexes inhibits the transfer of electrons from the electrode surface. In the range of 1–100 000 mU mL^{-1}, the logarithmic value of the CA19-9 concentration showed a good linear relationship with the peak current, and the linear equation is

$$\Delta I = 27.79 \log C_{\text{CA19-9}} + 11.63 \ (R^2 = 0.998)$$

where I (μA) is the peak oxidation current and C (mU mL^{-1}) is the CA19-9 concentration, with a linear range of 1 mU mL^{-1} to 100 000 mU mL^{-1} and a detection limit of 0.34 mU mL^{-1} ($3\delta/S$, δ is the standard deviation of the blank and S is the slope of the

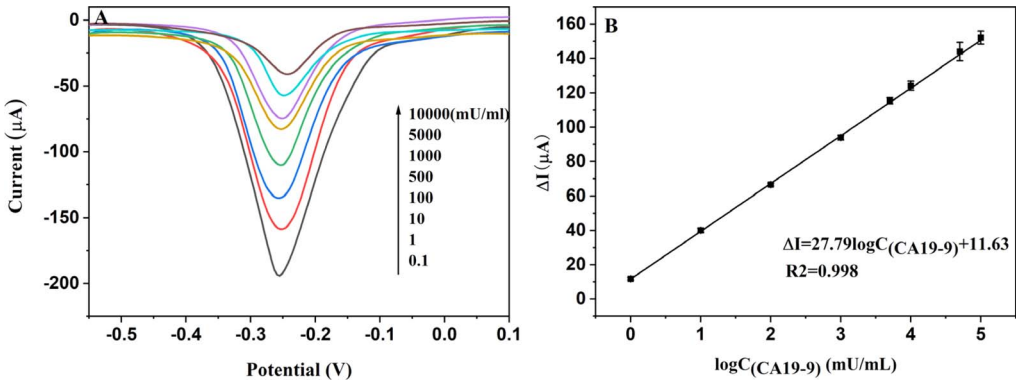

Fig. 4 (A) Response curve of DPV peak current to CA19-9 of different concentrations. (B) The working curves of declining values of peak current.

Table 1 Comparision of the proposed assay with some reported methods

Material	Technique	Linear range (mU mL^{-1})	Detection (mU mL^{-1})	References
Au-MoO_3–chitosan/porous graphene nanocomposite	SWV	2.5–1000	1	41
1DMoS_2 nanorods/$LiNb_3O_8$ and AuNPs@POM	DPV	0.0001–0.01	0.00003	8
g-C3N4@PtNPs and luminol-AgNPs@ZIF-67	ECL	0.1–10 000	0.16	42
PDA-Ag NPs@GO-MA	LSV	0.1–100 000	0.032	43
AuAg hollow nanocrystals	DPV	1000–30 000	228	44
rGO@Ce-MOF-on-Fe-MOF@Tb	DPV	1–100 000	0.34	This work

working curve). As shown in Table 1, this sensor has a wide linear range and very low detection limit compared to other reported sensors used for the determination of CA19-9. The excellent performance of the sensor is mainly due to the large specific surface area and porous structure of rGO@Ce-MOF-on-Fe-MOF@Tb, which can provide many binding sites for CA19-9 to amplify the electrochemical detection signal.

3.7. Stability, reproducibility and selectivity of the immunosensor

To investigate the stability of the immunosensor, we conducted consecutive CV scans on the modified electrodes. Scanning was performed to evaluate the short-term stability of the sensor, and as depicted in Fig. 5A, there was only a marginal decrease of 5.1% in the peak oxidation current value after 20 cycles of CV

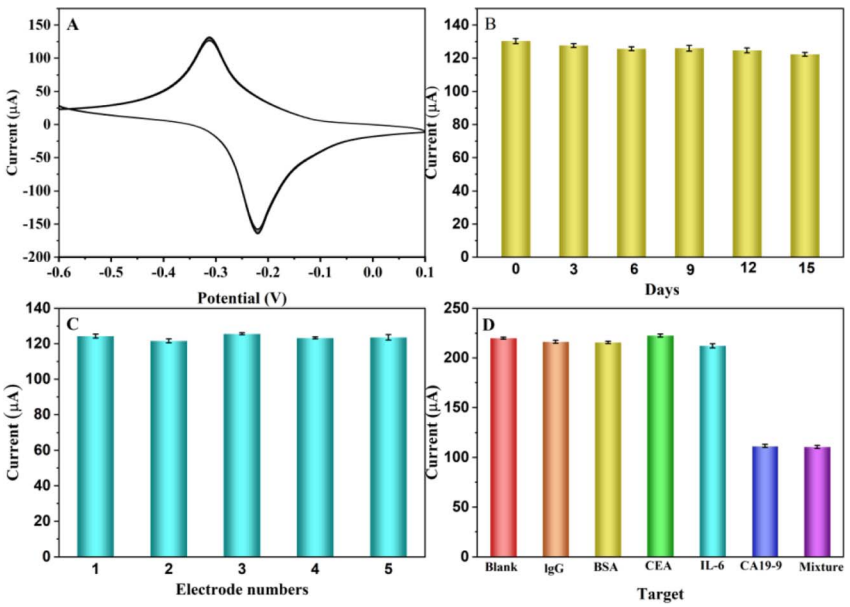

Fig. 5 (A) Stability of the immunosensors continuously scanned 20 cycles in 0.1 M PBS (pH 7.0) at a scan rate of 100 mV s^{-1} from −0.6 to 0.1 V. (B) Long-term stability of the immunosensors. (C) Reproducibility of the immunosensors based on five different electrodes incubated with 0.1 U mL^{-1} CA19-9. (D) Selectivity of the immunosensors with different interfering substances.

Table 2 Recovery of the prepared immunosensor

Sample	Added CA19-9 (mU mL^{-1})	Found (mU mL^{-1})	Recovery (%)	RSD (%)
1	10	9.82	98.20	3.6
2	100	103.21	102.21	2.8
3	500	506.18	101.24	1.9
4	1000	987.35	98.74	2.5
5	5000	4886.24	97.66	3.1

scanning. Furthermore, Fig. 5B illustrates the long-term stability results. The constructed immunosensor was stored at 4 °C for 15 days, and measurements were conducted every 3 days, revealing minimal changes in the peak current value with a relative standard deviation (RSD) of merely 3.18%. These findings demonstrate the excellent stability of the immunosensor.

To assess the sensor's reproducibility, five independently modified electrodes were subjected to DPV measurements under identical experimental conditions. As depicted in Fig. 5C, all electrodes exhibited comparable peak currents with a calculated RSD of 3.11%, indicating a high level of reproducibility for the sensor.

The selectivity of the rGO@Ce-MOF-on-Fe-MOF@TB-based immunosensor was assessed by conducting control experiments with potential interfering proteins (IgG, BSA, CEA, and IL-6), as depicted in Fig. 5D. Notably, the concentration of CA19-9 (0.1 U mL^{-1}) was significantly lower than that of the interfering protein (1 μg mL^{-1}). As shown in Fig. 5D, the signal responses of the various interfering substances resembled those of the blank solution. However, the modified electrodes incubated with CA19-9 exhibited a distinct DPV response similar to that observed for the mixture. These findings demonstrate the excellent selectivity of our developed immunosensor for detecting CA19-9 even in complex environments.

3.8. Analysis of real samples

To demonstrate the utility and feasibility of the immunosensor, we conducted recovery experiments by adding different concentrations of CA19-9 to human serum. The serum was diluted with 0.1 M PBS at a volume ratio 1 : 99. Different concentrations (10, 100, 500, 1000, and 5000 mU mL^{-1}) of CA19-9 antigen standard solutions were added and measured through the electrochemical method described previously. The obtained results are presented in Table 2. RSDs were calculated for each spiked solution, yielding recoveries ranging from 98.20% to 102.21% with RSD values below 4%. Thus, the proposed electrochemical immunosensor based on rGO@Ce-MOF-on-Fe-MOF@Tb holds great promise for real sample detection of CA19-9.

4. Conclusions

In this experiment, we synthesized two novel composite nanomaterials: rGO@Ce-MOF-on-Fe-MOF@Tb and rGO@Fe-MOF-on-Ce-MOF@Tb, which served as substrates for immobilized antibodies and the cancer marker CA19-9. Unlike the constrained layer-by-layer structure of Fe-MOF-on-Ce-MOF, Ce-MOF infiltrated into Fe-MOF in Ce-MOF-on-Fe-MOF to form a heterogeneous structure due to the relatively large pore size of Fe-MOF, thereby effectively integrating the advantages of both monomolecular MOFs. The immunosensor based on rGO@Ce-MOF-on-Fe-MOF@Tb demonstrated enhanced conductivity and superior stability for antigen–antibody immobilization compared to other immunosensors. Our results revealed that the proposed unlabelled immunosensor using rGO@CeMOFon-FeMOF-Tb exhibited a wide linear range (1–100 000 mU mL^{-1}), a low detection limit (0.34 mU mL^{-1}), excellent stability, reproducibility, repeatability, and satisfactory applicability; thus providing a promising platform for clinical applications.

Data availability

All relevant data are within the manuscript and its additional files.

Author contributions

According to the CRediT taxonomy: Tongxiao Zhao: conceptualization, methodology, formal analysis, investigation, data curation, writing – original draft. Baokang Jin: supervision, project administration, funding acquisition, conceptualization, validation, writing – review & editing, supervision. All authors have read and agreed to the published version of the manuscript.

Conflicts of interest

The authors declare that there are no conflicts of interest.

Acknowledgements

This work was supported by the National Nature Foundation of China (Grant 22076001 and 22376001).

References

1 S. A. Bannon, M. F. Montiel, J. B. Goldstein, W. L. Dong, M. E. Mork, E. Borras, M. Hasanov, G. R. Varadhachary, A. Maitra, M. H. Katz, L. Feng, A. Futreal, D. R. Fogelman, E. Vilar and F. McAllister, *Cancer Prev. Res.*, 2018, **11**, 679–686.
2 Y. Ono, Y. Inoue, H. Ito, T. Sasaki, T. Takeda, M. Ozaka, N. Sasahira, M. Hiratsuka, K. Matsueda, A. Oba, T. Sato, A. Saiura and Y. Takahashi, *Hpb*, 2023, **25**, 100–108.
3 J. W. Lee, J. H. Lee, Y. Park, J. Kwon, W. Lee, K. B. Song, D. W. Hwang and S. C. Kim, *J. Clin. Med.*, 2021, **10**, 1345.
4 B. Piro and S. Reisberg, *Sensors*, 2017, **17**, 794.
5 L. Jiao, Z. Mu, C. Zhu, Q. Wei, H. Li, D. Du and Y. Lin, *Sens. Actuators, B*, 2016, **231**, 513–519.
6 M. Chen, A. Qileng, H. Liang, H. Lei, W. Liu and Y. Liu, *Compr. Rev. Food Sci. Food Saf.*, 2023, **22**, 1285–1311.

7 R. Cancelliere, A. Di Tinno, A. Cataldo, S. Bellucci, S. Kumbhat and L. Micheli, *Microchem. J.*, 2023, **191**, 108868.
8 M. L. Yola and N. Atar, *Microchem. J.*, 2021, **170**, 106643.
9 T. Zhang, Y. Ma and Y. Zhang, *Analyst*, 2023, **148**, 5905–5914.
10 Y. Chen, X.-Z. Meng, H.-W. Gu, H.-C. Yi and W.-Y. Sun, *Biosens. Bioelectron.*, 2019, **134**, 117–122.
11 W. Zhang, R. Wang, F. Luo, P. Wang and Z. Lin, *Chin. Chem. Lett.*, 2020, **31**, 589–600.
12 Y. Ruan, H. Cai, J. Feng, H. Lei and H. Zheng, *Ionics*, 2024, **30**, 769–778.
13 N. Zhou, F. Su, C. Guo, L. He, Z. Jia, M. Wang, Q. Jia, Z. Zhang and S. Lu, *Biosens. Bioelectron.*, 2019, **123**, 51–58.
14 J. Xie, Z. Mu, B. Yan, J. Wang, J. Zhou and L. Bai, *Microchim. Acta*, 2021, **188**, 404.
15 M. Wang, M. Hu, Z. Li, L. He, Y. Song, Q. Jia, Z. Zhang and M. Du, *Biosens. Bioelectron.*, 2019, **142**, 111536.
16 X. G. Feng, S. R. Lin, M. Li, X. J. Bo and L. P. Guo, *Anal. Chim. Acta*, 2017, **984**, 96–106.
17 B. Makgabutlane, L. N. Nthunya, M. S. Maubane-Nkadimeng and S. D. Mhlanga, *J. Environ. Chem. Eng.*, 2021, **9**, 104736.
18 T. Georgiou, R. Jalil, B. D. Belle, L. Britnell, R. V. Gorbachev, S. V. Morozov, Y.-J. Kim, A. Gholinia, S. J. Haigh, O. Makarovsky, L. Eaves, L. A. Ponomarenko, A. K. Geim, K. S. Novoselov and A. Mishchenko, *Nat. Nanotechnol.*, 2013, **8**, 100–103.
19 M. C. Lemme, S. Wagner, K. Lee, X. Fan, G. J. Verbiest, S. Wittmann, S. Lukas, R. J. Dolleman, F. Niklaus, H. S. J. van der Zant, G. S. Duesberg and P. G. Steeneken, *Research*, 2020, **2020**, 8748602.
20 D. J. Buckley, N. C. G. Black, E. G. Castanon, C. Melios, M. Hardman and O. Kazakova, *2d Materials*, 2020, **7**, 032002.
21 A. P. F. Turner, *Chem. Soc. Rev.*, 2013, **42**, 3184–3196.
22 C. Xue, Q. Han, Y. Wang, J. Wu, T. Wen, R. Wang, J. Hong, X. Zhou and H. Jiang, *Biosens. Bioelectron.*, 2013, **49**, 199–203.
23 S. Prakash, T. Chakrabarty, A. K. Singh and V. K. Shahi, *Biosens. Bioelectron.*, 2013, **41**, 43–53.
24 C. Zhang, Y. Xu, C. Lv, X. Zhou, Y. Wang, W. Xing, Q. Meng, Y. Kong and G. Chen, *ACS Appl. Mater. Interfaces*, 2019, **11**, 29917–29923.
25 L. W. Mi, Q. Ding, W. H. Chen, L. Zhao, H. W. Hou, C. T. Liu, C. Y. Shen and Z. Zheng, *Dalton Trans.*, 2013, **42**, 5724–5730.
26 K. Liu, H. You, G. Jia, Y. Zheng, Y. Huang, Y. Song, M. Yang, L. Zhang and H. Zhang, *Cryst. Growth Des.*, 2010, **10**, 790–797.
27 A. C. Soares, J. C. Soares, F. M. Shimizu, V. D. Rodrigues, I. T. Awan, M. E. Melendez, M. H. O. Piazzetta, A. L. Gobbi, R. M. Reis, J. Fregnani, A. L. Carvalho and O. N. Oliveira, *Analyst*, 2018, **143**, 3302–3308.
28 L. Wang, J. Fu, Y. Chen and H. Ou, *J. Solid State Chem.*, 2022, **313**, 123297.
29 R. Ramachandran, W. Xuan, C. Zhao, X. Leng, D. Sun, D. Luo and F. Wang, *RSC Adv.*, 2018, **8**, 3462–3469.
30 T. D. Pollard, J. J. Ong, A. Goyanes, M. Orlu, S. Gaisford, M. Elbadawi and A. W. Basit, *Drug Discovery Today*, 2021, **26**, 69–79.
31 H. Yin, J. Zhu, J. Chen, J. Gong and Q. Nie, *Mater. Lett.*, 2018, **221**, 267–270.
32 X. Zhang, F. Hou, Y. Yang, Y. Wang, N. Liu, D. Chen and Y. Yang, *Appl. Surf. Sci.*, 2017, **423**, 771–779.
33 H. Yu, J. Han, S. An, G. Xie and S. Chen, *Biosens. Bioelectron.*, 2018, **109**, 63–69.
34 Z. Li, X. Liu, W. Jin, Q. Hu and Y. Zhao, *J. Colloid Interface Sci.*, 2019, **554**, 692–704.
35 R. Chen, J. Yao, Q. Gu, S. Smeets, C. Baerlocher, H. Gu, D. Zhu, W. Morris, O. M. Yaghi and H. Wang, *Chem. Commun.*, 2013, **49**, 9500–9502.
36 Y. Wang, Y. Zhang, D. Wu, H. Ma, X. Pang, D. Fan, Q. Wei and B. Du, *Sci. Rep.*, 2017, **7**, 42361.
37 S. Eissa and M. Zourob, *Nanoscale*, 2012, **4**, 7593–7599.
38 M. Lu, S. Kong, S. Yan, P. Zhou, T. Yu and Z. Zou, *J. Mater. Chem. A*, 2022, **10**, 12391–12399.
39 S. Wei, H. Xiao, L. Cao and Z. Chen, *Biosensors*, 2020, **10**, 24.
40 T. Anusha, K. S. Bhavani, J. V. S. Kumar, P. K. Brahman and R. Y. A. Hassan, *Bioelectrochemistry*, 2022, **143**, 107935.
41 S. Cotchim, S. Kongkaew, P. Thavarungkul, P. Kanatharana and W. Limbut, *Talanta*, 2024, **272**, 125755.
42 G. Mo, X. He, D. Qin, S. Meng, Y. Wu and B. Deng, *Biosens. Bioelectron.*, 2021, **178**, 113024.
43 N. Zhang, D. Zhang, C. Chu and Z. Ma, *Anal. Chim. Acta*, 2020, **1093**, 43–51.
44 R. Wang, J.-J. Feng, W.-D. Liu, L.-Y. Jiang and A.-J. Wang, *Biosens. Bioelectron.*, 2017, **96**, 152–158.

